Controlled rotation and translation of spherical particles or living cells by surface acoustic waves

Ianis Bernard, Alexander A. Doinikov, Philippe Marmottant, David Rabaud, Cédric Poulain, Pierre Thibault

Controlled rotation and translation of spherical particles or living cells by Surface Acoustic Waves.†

Ianis Bernard,[a] Alexander A. Doinikov,[a] Philippe Marmottant,[a] David Rabaud,[b] Cédric Poulain[b] and Pierre Thibault[a]‡

We show experimental evidence of the acoustically-assisted micromanipulation of small objects like solid particles or blood cells, combining rotation and translation, using high frequency surface acoustic waves. This was obtained from the leakage in a microfluidic channel of two standing waves arranged perpendicularly in a $LiNbO_3$ piezoelectric substrate working at 36.3 MHz. By controlling the phase lag between the emitters, we could, in addition to translation, generate a swirling motion of the emitting surface which, in turn, led to the rapid rotation of spherical polystyrene Janus beads suspended in the channel and of human red and white blood cells up to several rounds per second. We show that these revolution velocities are compatible with a torque caused by the acoustic streaming that develops at the particles surface, like that first described by [Busse *et al.*, *JASA*, 1981, **69** (6), 1634]. This device, based on standard interdigitated transducers (IDTs) adjusted to emit at equal frequencies, opens a way to a large range of applications since it allows the simultaneous control of the translation and rotation of hard objects, as well as the investigation of the response of cells to shear stress.

1 Introduction

Non contact methods to manipulate small particles or cells are of major importance due to the increasing need to perform elementary operations like moving, assembling or sorting objects in microfluidic devices. One strategy is to generate at the scale of these objects forces that counterbalance viscous effects [1] caused by the surrounding fluid, namely Stokes' force. These include dielectrophoretic [2], diamagnetic [3] or acoustic [4] effects and, at smaller scale, electric gradients to trap dielectric particles [5]. It has for instance been demonstrated that acoustical tweezers based on the emission of standing surface acoustic waves (SSAW) on piezoelectric wafers can be used to move particles, cells and even living microorganisms like *C. elegans* [6,7] in strong analogy with optical tweezers but with forces of larger amplitudes. Such labs on chips combine the advantages of size reduction due to the high acoustic frequency employed and transparency and biocompatibility offered by PDMS micro channels. Pushing forward the analogy between acoustics and optics, one may wonder if one could also generate acoustic torques in such devices. On the one hand, an acoustic wave being scalar in nature, there is no equivalent of the circular polarisation and spin angular momentum carried by an electromagnetic wave. On the other hand, it has been shown by Lord Rayleigh that radiation pressure can induce torques [8,9,10]. More recently, it has been shown that light and acoustic waves can both carry orbital angular momentum in particular if the *beam's phase fronts are not perpendicular to the propagation direction* [11,12,13,14] and rotations have been obtained from particles that absorb light [15] or that are birefringent [16].

We show in this article the rotation induced from leaky SAW generated on a $LiNbO_3$ substrate. Its origin is the acoustic streaming that develops at the surface of the particle if the surrounding *fluid* particles are imposed an elliptical motion due to the unique nature of the acoustic wave (see Fig. 7 in Lee *et al.* [17]). In addition, it is shown that the high frequency used in the experiment (above 35 MHz) allows tenths of micron size particles to be simultaneously put in motion in the same minute volume. These characteristics open new perspectives for labs on chips since torques used up to now to manipulate objects were obtained under action of bulk acoustic waves (BAW) [18] or evanescent waves [19] in the MHz range. Compared to optical tweezers, the transfer of momentum from acoustic streaming is an additional tool to generate torques for particles of various compositions and shapes and which have no equivalent in optics.

To investigate this phenomenon, we designed an experimental setup where four interdigitated transducers (IDTs) emitting at the same frequency generate two pairs of orthogonal SAW that leak in a microfluidic volume. By dexterously adjusting the phase between emitters, we could, firstly, control the acoustic minima in which particles are trapped and impose a position, and, secondly, their rotation. These rotations are evidenced on spherical

[a] *CNRS / Université Grenoble-Alpes, LIPhy UMR 5588, Grenoble, F-38401, France.*
[b] *Univ. Grenoble Alpes, CEA, LETI MINATEC Campus, F-38000 Grenoble, France.*
† Electronic Supplementary Information (ESI) available: Supporting information and movies. See DOI: 10.1039/b000000x/
‡ corresponding author. E-mail: Pierre.Thibault@univ-grenoble-alpes.fr. Tel: +33 (0)668 104 915. Fax: +33 (0)476 635 495;

objects like semi-metalised spherical polystyrene beads (hereafter designed as *Janus beads*) and blood cells. The angular velocity is seen to depend on the sine of the phase lag between the two orthogonal SAWs and on the product of the pressure amplitudes. For particles with positive acoustophoretic factors[20], the torque appears to be maximum at the pressure nodes, *i.e.* in the locations where the particles are trapped, with alternate clockwise and anti-clockwise directions of rotation.

2 Working mechanism

The principle of acoustic torque generation using SSAW relies first on the forcing of circular orbits of fluid particles in the microfluidic channel plane, around pressure nodes columns in which solid particles accumulate. Acoustic streaming develops at the surface of a solid particle due to viscous effects and, if the stress distribution is not symmetrical, a total torque on the particle is produced inducing its rotation.[21] This mechanism is also responsible for the observation of strong recirculations in thin liquid films deposited on piezoelectric substrates.[22,23] In recent works aiming at developing acoustic tweezers[24,25] it has been shown that vortex beams produced from the swirling surface waves created on piezoelectric substrates can indeed force such circular orbits. In addition, the mechanism by which acoustic torques are generated from acoustic streaming has been shown at macroscale.[17,26] However, there was not yet evidence that small solid particles could be put into rotation. A reason is that the high frequency (>30 MHz) used for SAW leads to a viscous length δ_η as small as 0.1 µm, questioning the ability of acoustic streaming to produce significant torques. In the present experiment, the acoustic field is generated by four IDTs exciting the piezoelectric surface of a $LiNbO_3$ substrate (see Figs. 1a and 4) along its two perpendicular main axes. The swirling of the surface is obtained by introducing a temporal phase lag φ between the two standing waves, leading to a complex pressure field just above the active surface of the form

$$\underline{p}_{\text{in}}(x,y,t) = \left[p_{0x}\sin(k_x x) + p_{0y}\sin(k_y y)\exp(i\varphi)\right]\exp(-i\omega t) \quad (1)$$

with p_{0x} and p_{0y} the pressure amplitudes along axis $\mathbf{e}_x$ and $\mathbf{e}_y$ and k_x and k_y the wave numbers, which are generally different due to the crystal anisotropy.[27,28,29] Since the wave velocities at the surface are larger than that in the liquid (supersonic regime), the surface waves will propagate and attenuate in the fluid volume, building a 3D pressure field of standing waves more complex that the 2D model associated to eqn (1), and importantly with interferences between the two orthogonal directions due to the phase lag term. This role of φ is illustrated in Fig. 1b where we show the time evolution of the pressure field emitted at the surface of a piezo material in the ideal case $\varphi = \pi/2$, at different times of the period T, creating a swirling evolution of the wave front around the central pressure node. For comparison, we show the same pressure field corresponding to a Bessel beam of order $m = 1$ in Fig. 1c, which general expression for the spatial part of pressure field in cylindrical coordinates and for a isotropic material with $k = k_x = k_y$ is

$$\underline{p}(\rho,\alpha,z) = p_0 J_m(k\rho)e^{i(m\alpha+k_z z)} \quad (2)$$

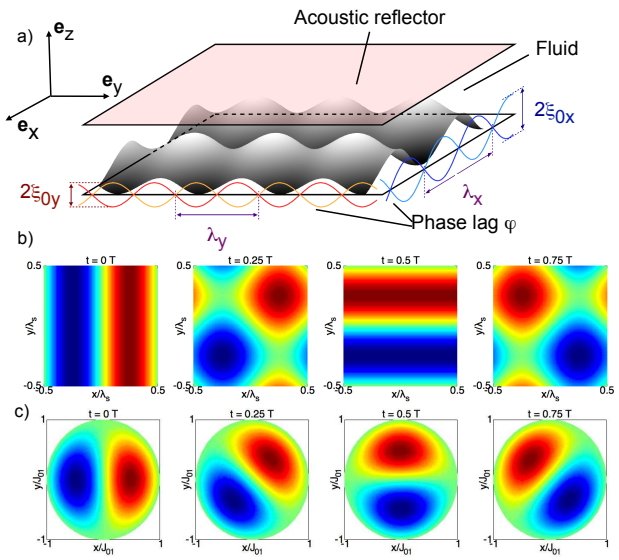

Fig. 1 a) Scheme of the 3D model under consideration: 2 orthogonal SSAW are generated on the crystal surface with a time phase lag φ. The waves emitted in the liquid are perfectly reflected at the channel top located at $z = h$ and propagate parallel to the lower surface with wave vectors $\mathbf{k}_x$ and $\mathbf{k}_y$. b) and c) Scheme of the time evolution (T is the period) of the pressure field in the plane of the source in the case of: b) four emitters with a phase lag $\varphi = \pi/2$ between the two orthogonal directions. Cell extension $\lambda_s \times \lambda_s$. c) a vortex beam of order 1. The radial extension is 1 since it has been normalized by the first zero of the Bessel function.

with J_m the Bessel function of radial order m. Similarly to orthogonal waves, a screw dislocation[30,31] is observable around the origin, though the overall shape is different at some distance from the center. To further illustrate this mechanism, we show on Movie S1 (see ESI†) the oscillations of a surface of lateral extent one wave length λ_s considering for simplicity $\lambda_x = \lambda_y$ for various amplitude ratios and phase lags between the two waves: Lissajous figures are observed close to each pressure node. Remarkably, while the distance between pressure nodes is $\lambda_s/2$, the helicity is alternatively left and right, leading to a total period λ_s.

Let now consider the position of particles in a 3D micro channel. A first approximation of the pressure field in the volume of the acoustic cavity is to see it as an extension of a 2D in-plane problem. If one considers hard particles in water, of radius r_0 small respective to the wavelength in the fluid ($r_0 < \lambda_f$), their acoustophoretic factors being positive, they would tend to be trapped in columns above the pressure nodes in the liquid channel by the partially reflected wave, but also to be pushed against the to wall. The introduction of a reflector leads to similar results, with particles now clearly separated by $\lambda_f/2$ in the z direction. At the same time the particles are trapped, the pressure wave oscillation will also be responsible for the acoustic streaming, developing tangentially to the particle surface. To evaluate the subsequent stress on the particles, one can notice that in a $x-y$ levitation plane, this situation indeed resembles that considered by Lee *et al.*[17] of two orthogonal waves with a phase lag φ. However, instead of considering macroscopic objects and a viscous penetration length δ_η in the millimeter range associated to

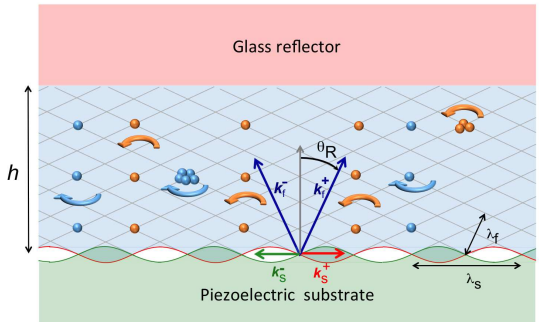

Fig. 2 Scheme of the propagation of a leaky SAW and of the suspension of rotating objects. Surface acoustic waves are emitted from left and right from the piezo surface, with wave vectors in the solid denoted $\mathbf{k}_s^+$ and $\mathbf{k}_s^-$. In contact with the liquid, a leakage occurs of the sound waves with wave vectors in the fluid $\mathbf{k}_f^+$ and $\mathbf{k}_f^-$ emitted at the Rayleigh angle θ_R from the normal. The presence or absence of a reflector may lead to total or partial reflection of the wave at the upper boundary leading to the creation of a total or partial standing wave in the channel height.

kHz frequency, it will be of the order of 0.1 µm while r_0 is in the 10 µm range. Eventually, in order to evaluate the amplitude of the rotation velocity of a particle of given diameter, one should compute the viscous torque opposing the driving acoustic torque. For this purpose, we consider for simplicity a sphere of radius r_0 at the center of an orthonormal frame so that the zenithal direction is along $\mathbf{e}_z$ while $\mathbf{e}_x$ and $\mathbf{e}_y$ are aligned with the standing wave directions. We then define a spherical coordinate system of polar angle θ and azimuth ψ. According to Refs [17,26], the components of the streaming velocity $\mathbf{u}_L$ immediately outside the boundary layer are tangent to the sphere, with components along directions $\mathbf{e}_\theta$ and $\mathbf{e}_\psi$ equal to:

$$u_L = \frac{45}{16\omega r_0 \rho_0^2 c_0^2} \times \Big[\Big(p_{0x}^2\cos^2(k_x x)\cos^2(\psi) + p_{0y}^2\cos^2(k_y y)\sin^2(\psi)\Big)\sin(\theta)\cos(\theta) + 2p_{0x}p_{0y}\cos(\varphi)\cos(k_x x)\cos(k_y y)\sin(\theta)\cos(\theta)\sin(\psi)\cos(\psi)\Big] \quad (3)$$

and

$$v_L = \frac{45}{16\omega r_0 \rho_0^2 c_0^2} \times \Big[-\Big(p_{0x}^2\cos^2(k_x x) - p_{0y}^2\cos^2(k_y y)\Big)\sin(\theta)\cos(\psi)\sin(\psi) + p_{0x}p_{0y}\cos(\varphi)\cos(k_x x)\cos(k_y y)\sin(\theta)\cos(2\psi) + \frac{6}{5}p_{0x}p_{0y}\sin(\varphi)\cos(k_x x)\cos(k_y y)\sin(\theta)\Big] \quad (4)$$

where ρ_0 is the fluid density, c_0 the sound velocity in the fluid, ω the circular frequency of the time harmonic fields. The velocity amplitudes corresponding to streaming are of second order respective to the acoustic field, and can be expressed as a function of the first order velocity v_1. Assuming $p_{0x} = p_{0y} = p_0$, we get $v_1 \sim p_0/\rho_0 c_0$ and

$$u_2 \propto \frac{45}{16}\frac{p_0^2}{\omega r_0 \rho_0^2 c_0^2} \propto \frac{45}{16}\frac{v_1^2}{\omega r_0} \quad (5)$$

Accordingly, the components of the surface stress experienced by the particle are given by:

$$\mu\left(\frac{\partial u_2}{\partial r}\right)_{r=r_0} = -\frac{9}{16\rho_0 c_0^2}\frac{\delta_\eta}{r_0} \times \Big[\Big(p_{0x}^2\cos^2(k_x x)\cos^2(\psi) + p_{0y}^2\cos^2(k_y y)\sin^2(\psi)\Big)\sin(\theta)\cos(\theta) + 2p_{0x}p_{0y}\cos(\varphi)\cos(k_x x)\cos(k_y y)\sin(\theta)\cos(\theta)\sin(\psi)\cos(\psi)\Big] \quad (6)$$

and

$$\mu\left(\frac{\partial v_2}{\partial r}\right)_{r=r_0} = \frac{9}{16\rho_0 c_0^2}\frac{\delta_\eta}{r_0} \times \Big[\Big(p_{0x}^2\cos^2(k_x x) - p_{0y}^2\cos^2(k_y y)\Big)\sin(\theta)\cos(\psi)\sin(\psi) - p_{0x}p_{0y}\cos(\varphi)\cos(k_x x)\cos(k_y y)\sin(\theta)\cos(2\psi) + 2p_{0x}p_{0y}\sin(\varphi)\cos(k_x x)\cos(k_y y)\sin(\theta)\Big] \quad (7)$$

As shown by Lee *et al.* [17], only the last term of eqn (7) contributes to the total torque on the sphere, and its amplitude in the case of a 2D standing wave depends on its position in the channel. For a particle at coordinates (x,y,z) where z is a levitation plane, this driving torque is expressed by:

$$\Gamma^{\text{streaming}} = \frac{3\pi r_0^2 \delta_\eta}{\rho_0 c_0^2} p_{0x}p_{0y}\cos(k_x x)\cos(k_y y)\sin(\varphi)\mathbf{e}_z \quad (8)$$

These streaming velocities and surface stresses are represented in Fig. 3. As expected, when φ=0, the effective torque is null from symmetry consideration, while its amplitude reaches a maximum when $\varphi = \pm\pi/2$. More generally, we expect the particle to rotate at a velocity given by u_2 modulated by a term proportional to $\sin(\varphi)$. To continue the analogy with acoustical vortex beams [31], the previous situation can be treated as having four emitters arranged on a cross shape, that are spatially turned by $\pi/2$, while their relative phases are also increased by $\pi/2$ when turning around the center, explaining the swirling of the surface and the physical origin of the torque.

3 Materials and methods

3.1 Device fabrication

The high frequency acoustic setup used to generate the simultaneous translation and rotation of particles is sketched in Fig. 4a. It is obtained by assembling a soft PDMS microfluidic channel onto a $LiNbO_3$ wafer on which thin electrodes have been evaporated to make interdigitated transducers (IDTs). Since the properties of a piezoelectric $LiNbO_3$ crystal are highly anisotropic [32],

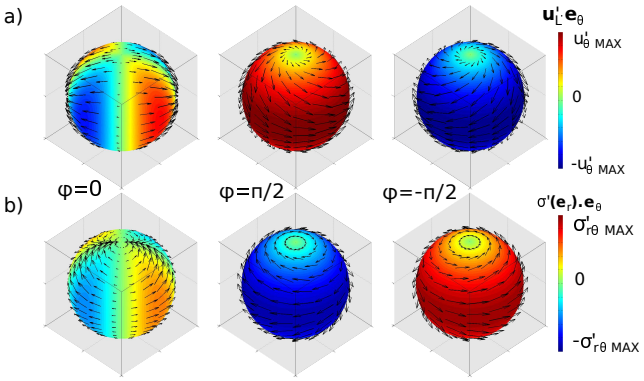

Fig. 3 Illustration of the action of the acoustic streaming developing at the surface of a small sphere due to two orthogonal waves with phase lag φ assuming similar pressure amplitudes $p_{0x} = p_{0y}$. a) Velocity field at a distance δ_η from the wall [17], for three different values of the phase $\varphi = 0, \pm\pi/2$. b) Acoustic streaming stress field components. The color code reflects the amplitude of the horizontal component of the vector field (i.e. along the azimuth).

a X-cut [27,33,34] is chosen as it gives high electromechanical coupling coefficients in the two crystal directions Y ($K^2_Y = 3.58\%$, Rayleigh wave celerity $c^R_Y = 3750\,$m/s, aligned along x) and Z ($K^2_Z = 5.00\%$, celerity $c^R_Z = 3481\,$m/s, aligned along y). The IDTs, made of fifty finger pairs with respective pitches $\lambda_x = 100.0\,\mu$m and $\lambda_y = 93.9\,\mu$m and a minimal metallization ratio of 50% (up to 80% for the best results), have been designed to have their maximum emission at the same resonance frequency of 36.3 MHz when loaded with water with impedances close to 50 Ω. The experimental chamber is made by soft lithography techniques, by pouring PDMS on a 150 µm thick resin pattern corresponding to the 1.2×1.2 mm microfluidic chamber, inlet and outer channels and four pads that will located above the IDTs in order to leave voids. These IDTs have an aperture of 1.6 mm (total width 1.9 mm), covering the physical size of the acoustic chamber, with a distance between opposite pairs of IDTs of 2.6 mm (see Fig. 4c). In most experiments, a thin microscope circular coverslip is used to cover the microfluidic chamber and the pads. This prevents the collapse of the PDMS over the IDTs and allows one building a reflector for the acoustic cavity. After curing, the thin PDMS between the acoustic chamber and the glass coverslip is peeled off and the microfluidic channel is assembled on the $LiNbO_3$ using an oxygen plasma bonding (see Fig. 4d). Since the voids in the PDMS exceeds the IDTs dimension by 100 µm, the SAW travel a distance of PDMS of about 600 µm before reaching the acoustic cavity leading to a decrease in amplitude of about 15%, according to the attenuation coefficient of 290 m^{-1} we measured with a network analyzer (HP Model 4195A). Additional transmission measurements show that a 5 mm thick PDMS entirely covering the IDTs distant by 3.5 mm leads to a tenfold attenuation of the transmission compared to the unloaded wafer. We show in Fig. 5a the electrical response measured on a 3" wafer with electrodes made of aluminum: a mechanical resonance is clearly present close to 37 MHz, with additional rapid oscillations due to the existence of bulk acoustic waves of less amplitude (but which become dominant above 50 MHz). With a PDMS micro channel deposited

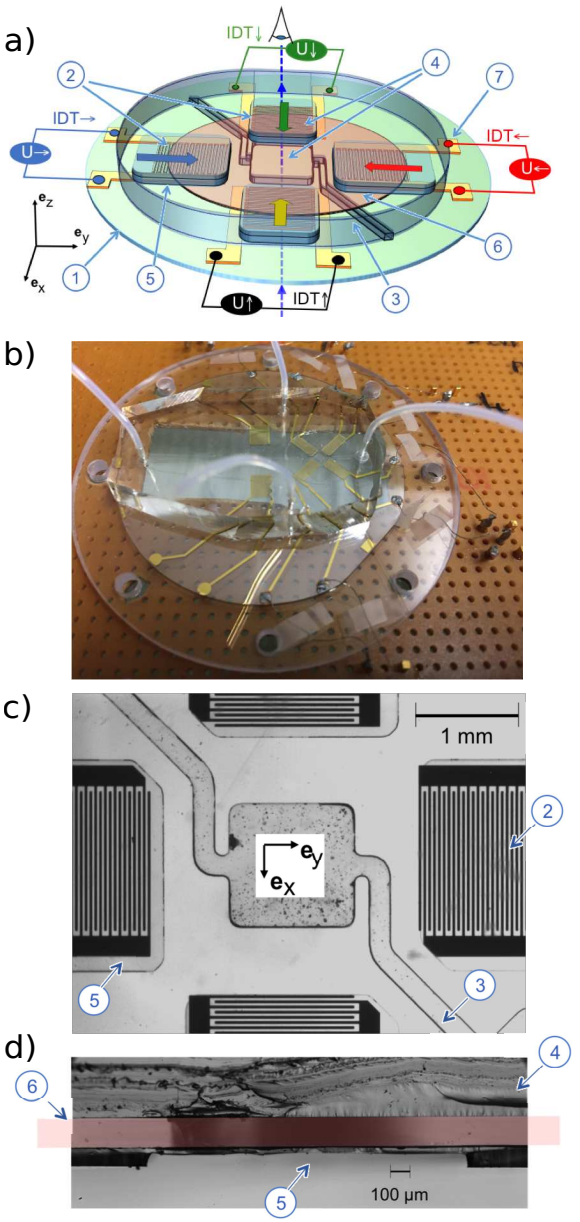

Fig. 4 Typical microfluidic setup. Legend: **1**- X-cut $LiNbO_3$ wafer, 1 mm thick, diam. 2". **2**–10 nm Ti-100 nm Au IDTs. **3**-100 µm×200 µm micro channel. **4**-PDMS. **5**-Voids in PDMS. **6**-⌀25 mm, 150 µm thick borosilicate coverslip. **7**- Connecting pads. a) Scheme of the acoustic device geometry. The acoustic chamber is 1.2 mm wide and 100 to 150 µm high. b) Photograph of the final experimental device showing the piece of PDMS assembled to the piezo substrate supported by a piece of plexiglass. One distinguishes the acoustic cavity in the middle of the IDTs and the glass coverslip on top. The electrical connections are obtained by connecting the IDTs to the pins of SMC connectors that stick out from a PCB. The additional IDTs at the left are not used in the experiment. c) Top-view of a dirty acoustic chamber and IDTs. d) Crosscut image with a zoom showing the void imprint left after molding the PDMS. The thin remaining PDMS layer is peeled off from the glass coverslip before assembly to fabricate the acoustic cavity.

on top of the wafer (but an empty acoustic chamber), these BAW modes are attenuated, and we mostly observe the typical response of SAW emitted by the IDTs. The electrical transmission is illustrated by Fig. 5b which shows that by adjusting the pitches and number of fingers of the IDT pairs along the weak Y and strong Z

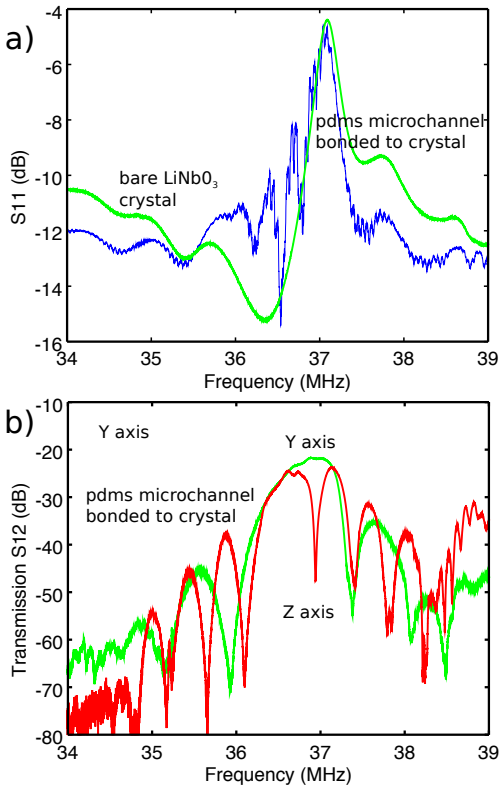

Fig. 5 Electrical characterization of IDT pairs obtained by depositing 10 nm of Ti+100 nm of Al on X-cut $LiNbO_3$ samples and designed to compensate for crystal anisotropy, with a mechanical resonance close to 37 MHz. Weak Y axis: pitch λ_x=100 µm, 84 finger pairs. Strong Z axis: pitch λ_y=93.9 µm, 50 finger pairs. a) ⌀3", 1 mm thick wafer. Blue curve: measurement of $|S_{11}|$ along the Y-axis for a bare sample. Green curve: $|S_{11}|$ along the Y-axis for a sample with a PDMS microfluidic channel containing a glass reflector on top. b) ⌀2", 500 µm thick wafer. Measured transmission $|S_{12}|$ between receiver and emitter along axes Y (green curve) and Z (red curve) with a PDMS microfluidic channel containing a glass reflector on top.

axis one can obtain similar electromechanical responses despite the strong crystal anisotropy for the same electrical voltages.

3.2 Methods

Depending on experiment, the microcavity is either filled with ⌀10 µm Janus particles suspended in a water/surfactant solution (see Movie S2† for illustration), or blood cells. Janus particles are half metalised yellow-green fluorescent carboxylate polystyrene microspheres (Fluoresbrite, Polysciences Inc.). They are obtained by diluting the microbeads in ethanol (3% in weight), and by further depositing 100 µL of this solution on a glass coverslip first exposed to 5 minutes to a O_2 plasma. After drying, 12 nm of titanium and then 38 nm of gold are evaporated on the sample, and beads are detached by dilution in water or ethanol using sonication. The suspended beads are then collected by centrifugation and used for experiments (see also Ref.[35]). Qualitative measurements on blood cells are performed using whole blood, removing platelets by centrifugation at about 1 000 g for 10 minutes and by diluting RBCs and WBCs in PBS. Quantitative measurements on RBCs are obtained after centrifugation and dilution 100 times in an isotonic and isodensity solution of PBS and Optiprep (AxisShield, Norway). The particle rotations are observed under an inverted microscope (Olympus, IX70) using a ×20 or ×40 magnification objective and are recorded with a high speed camera (Miro 4 or Miro 310, Vision Research), at 100 to 300 frames per second allowing 10 to 40 s recordings in order to average rotation speed over tenths of turns. The four IDTs are connected to the SMC panel mounts using ⌀80 µm copper wires using silver paste and tin solder (see Fig. 4b), and are excited by two synchronized dual channels arbitrary waveform generators (AFG3102C, Tektronix).

Initially, the efficiency of the IDTs is generally tested by applying a moderate voltage on one pair of IDTs, along $\mathbf{e}_y$ for instance, setting the frequency close to the resonance for the first ($f_y^{\rightarrow} = f_0$), while we impose a slight frequency modulation of typ. 1 Hz on the other ($f_y^{\leftarrow} = f_0 + \delta f$). This allows one to observe the organisation of small suspended particles due to radiation forces within the channel as well as to calibrate acoustic forces against Stokes drag.[6] A similar operation is performed on the second pair of IDTs until acoustic pressures p_{0x} and p_{0y} are balanced. Under such conditions, well organized square or triangular lattices of aggregated particles can be observed in the acoustic cavity, with some distortions due to diffraction effects in the near field emission of the IDTs. Eventually, voltages as low as 4 Vpp (16.0 dBm) can be used along the weak (Y) axis and 3 Vpp (13.5 dBm) for the strong (Z) direction, therefore requiring no power amplifier. Interestingly, these amplitudes are much less than that reported for the viability assays of Ref.[7] indicating that the acoustic field is likely to be compatible with living material. Rotation experiments are then performed by controlling the individual phase lag of each IDT, respective to $\phi_x^{\downarrow}$. In practice, a lot of efforts were devoted to obtain a system for which the amplitudes of the waves emitted by the IDTs in a given direction pair are only weakly dependent on the electrical phase. The reason is the electromechanical reflections that exist between each pair of IDTs, which can or cannot amplify the individual emission of each IDT, depending on their relative position. A simulation of this effect is presented in ESI†.

4 Rotation of acoustically trapped objects

4.1 Location of suspended particles

Like in large scale experiments[26], the observation of streaming induced rotation of particles is preferentially observed at the pressure nodes of the acoustic field, and is maximum when the two orthogonal standing waves are in quadrature. However, the position itself of the particle depends also on this phase lag, as we further show.

According to Gor'kov's derivation[20,36], for small enough particles respective to the sound wavelength (see Refs.[24,37] for the generalization to arbitrary particles), the acoustic force derives from an acoustic potential which writes:

$$\frac{U^{\mathrm{rad}}}{\mathscr{V}} = \frac{1}{2} f_1 \kappa_0 < \underline{p}_{\mathrm{in}}^2 > - \frac{3}{4} f_2 \rho_0 < \underline{\mathbf{v}}_{\mathrm{in}}^2 > \qquad (9)$$

with $\mathscr{V}$ the particle volume and where we have introduced the

acoustophoretic coefficients $f_1 = (\kappa_0 - \kappa_p)/\kappa_0$ and $f_2 = 2(\rho_p - \rho_0)/(2\rho_p + \rho_0)$ with κ_p and ρ_p (resp. κ_0 and ρ_0) the particle (resp. fluid) compressibility and density and where the brackets represent time averages of the sound wave. Considering two orthogonal waves with a phase lag φ, the velocity field associated to the pressure field given in eqn (1) writes

$$\underline{\mathbf{v}}_{\text{in}} = \frac{e^{-i\omega t}}{i\rho_0\omega}\left[p_{0x}k_x\cos(k_x x)\mathbf{e}_x + p_{0y}k_y\cos(k_y y)e^{i\varphi}\mathbf{e}_y\right] \tag{10}$$

and the total potential becomes:

$$\frac{U^{\text{rad}}}{\kappa_0\mathscr{V}} = \frac{f_1}{4}\left(p_{0x}^2\sin^2(k_x x) + p_{0y}^2\sin^2(k_y y) + 2p_{0x}p_{0y}\sin(k_x x)\sin(k_y y)\cos\varphi\right)$$
$$-\frac{3f_2}{8k_0^2}\left(p_{0x}^2k_x^2\cos^2(k_x x) + p_{0y}^2k_y^2\cos^2(k_y y)\right) \tag{11}$$

As a consequence, the acoustic potential between two orthogonal SSAW also depends on its phase lag φ via the pressure term of eqn (9) which is responsible for interferences. Note that according to the construction of Fig. 2, the ratio k_x/k_0 that appears in eqn (11) is due to the difference in sound velocities along directions $\mathbf{e}_x$ and $\mathbf{e}_y$. It simplifies for an hypothetic isotropic piezo material for which we would have $k_x = k_y = k_s$ with k_s the surface wave wavenumber. If in addition the acoustic amplitudes are set equal ($p_{0x} = p_{0y} = p_0$), eqn (11) reduces to:

$$\mathbf{F}^{\text{rad}} = -4\pi E_{\text{ac}}k_s r_0^3\left[\left(\Phi\sin(2k_x x) + \frac{2f_1}{3}\cos(k_x x)\sin(k_y y)\cos(\varphi)\right)\mathbf{e}_x\right.$$
$$\left. + \left(\Phi\sin(2k_y y) + \frac{2f_1}{3}\sin(k_x x)\cos(k_y y)\cos(\varphi)\right)\mathbf{e}_y\right] \tag{12}$$

where we have introduced the acoustic energy $E_{\text{ac}} = \kappa_0 p_0^2/4$ and the acoustophoretic coefficient $\Phi = \frac{1}{3}f_1 + \frac{1}{2}f_2$. For Janus particles in water, $f_1 = 0.44$, $f_2 = 0.03$ so that $\Phi \sim 0.162$[38], while for red/white blood cells in PBS $f_1 = 0.11$, $f_2 = 0.05$ so that $\Phi \sim 0.062$[39,40]. Since Φ is positive in both cases, the particles are always attracted to the pressures nodes. These locations correspond to the crosses in Fig. 6 where we have plotted the relative 2D potential amplitude of a levitation plane in the microchannel for different values of the phase lag. Due to interference terms, the potential is seen to have elongated minima with a period $\lambda_s/2$ in the case $\varphi = 0$, and evolves toward a regular diamond structure square lattice structure for $\varphi = \pm\pi/2$, as visible in Fig. 7.

In the case the two orthogonal waves are not of the same amplitude, the potential shows some preferred directions for particle alignement. By contrast, acoustic torques have a λ_s periodic structure, since the rotation alternates left and right every $\lambda_s/2$. This can be seen by seeding a water flow with micron-size particles which will form aggregates. This is further evidenced in the case of a coacervate solution we obtained by mixing ethyl alcohol, water, a surfactant and potassium iodine crystal, for which we observe low density micelles at pressure antinodes ($\Phi < 0$) whereas Janus particles rotate in pressure nodes. Of course, the actual 3D geometry of the acoustic cavity is more complex than this simple 2D approximation. In particular, while trapping columns still exist above the displacement nodes, the presence of standing waves in the channel height is responsible for levitation planes that build above displacement antinodes. These aspects are discussed in ESI†.

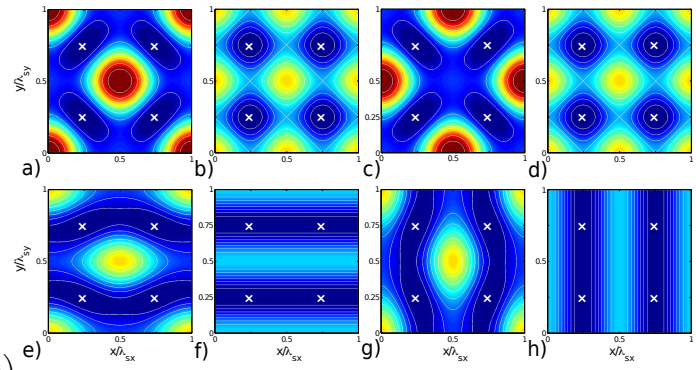

Fig. 6 Contour plot of Gor'kov's acoustic potential for PS beads in water. The minima are in blue while the maxima are in red. The same scale is used for all plots. Top: $p_{0x} = p_{0y}$ (a) $\varphi = 0$, (b) $\varphi = \pi/2$, (c) $\varphi = \pi$ and (d) $\varphi = 3\pi/2$. Bottom (φ=0): (e) $p_{0y} = 2p_{0x}$, (f) $p_{0x} = 0$, (g) $p_{0y} = p_{0x}/2$ and (h) $p_{0y} = 0$. The white crosses show pressure nodes that have been shifted from center to show a field size of dimensions $\lambda_s \times \lambda_s$.

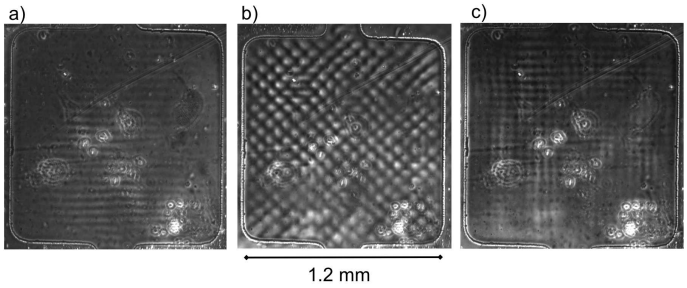

Fig. 7 Phase contrast images of a microfluidic cavity of dimensions 0.1 mm×1.2 mm×1.2 mm filled with ethanol and observed with a phase contrast microscope (The four IDTs are located sideways, as illustrated in Fig. 4, and the view is from the top). (a) Emission along $\mathbf{e}_x$, (b) Emission along $\mathbf{e}_x$ and $\mathbf{e}_y$, $\varphi = 0$, (c) Emission along $\mathbf{e}_x$ and $\mathbf{e}_y$, $\varphi = \pi/2$.

4.2 Torques measured on Janus beads

In order to validate quantitatively the previous model, we show in Fig. 8 the rotation velocity of ⌀10 µm Janus beads, normalized by their maximum velocity obtained for $\varphi = \pi/2$. The red and green data have been obtained by counting the rotations observed at different φ every 10°, and the error is typically 1 turn. Black squares are interpolated values obtained by continuously sweeping the phase, and we show mean and standard deviations. Comparing these data with the dotted blue line which is obtained by equating the viscous torque and the acoustic torque of eqn (8) (stationary rotation assumption), we observe a very good qualitative agreement. However, for some reason, we observed on the green, orange or red symbols an asymmetry between left and right rotation directions, which happens to be the case for most beads, with no statistically preferred direction in average. Typically, rotation velocities Ω up to 50 rad/s are measured for an applied voltage of only 20 dBm. Since the expression for the resistive viscous torque

on a sphere at low Reynolds number[41] is $\Gamma_\eta = 8\pi\eta r_0^3 \Omega \mathbf{e}_z$, one can relate the rotation velocity to the acoustic pressure by projecting the angular momentum equation along $\mathbf{e}_z$:

$$J\frac{d\Omega}{dt} = \Gamma^{\text{streaming}} - \Gamma_\eta \tag{13}$$

with J the moment of inertia of the particle. In steady state, the acoustic torque and the friction torque balance each other and using eqn (8), one obtains an estimate of the rotation velocity. Taking $\delta_\eta = 0.1\,\mu\text{m}$, and considering a Janus bead in water, one obtains $\Omega = 3\delta_\eta p_{0x} p_{0y} \sin\varphi / 8 r_0 \rho_0 c_0^2 \eta \simeq 3\,10^{-9} p_{0x} p_{0y}$. Reciprocally, the measured rotational velocities of order of 10 rps shown in Fig. 8 involve pressure field amplitudes $p_{0x} \sim p_{0y} \sim 1.4\,\text{bar}$, which is rather intense.

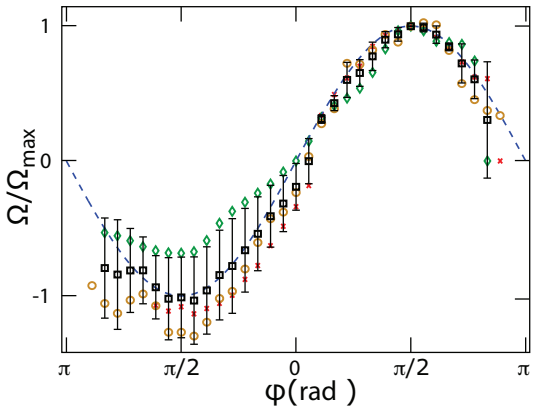

Fig. 8 Normalized rotation velocity of $10\,\mu\text{m}$ Janus beads. Red and green symbols: measurements of two different beads in a device with a glass reflector. IDTs along $\mathbf{e}_y$ and IDTs along $\mathbf{e}_x$ are connected to the same channel of the generator and the same phase lag is applied to $\text{IDT}_x^{\downarrow}$ and $\text{IDT}_x^{\uparrow}$ relative to $\text{IDT}_y^{\rightarrow}$ and $\text{IDT}_y^{\leftarrow}$. Green diamonds: $\text{IDT}_y^{\rightarrow}$ and $\text{IDT}_y^{\leftarrow}$: 4 Vpp, $\text{IDT}_x^{\downarrow}$ and $\text{IDT}_x^{\uparrow}$: 6 Vpp, Ω_{max}=5.4 rps. Red crosses: : $\text{IDT}_y^{\rightarrow}$ and $\text{IDT}_y^{\leftarrow}$: 6 Vpp, $\text{IDT}_x^{\downarrow}$ and $\text{IDT}_x^{\uparrow}$: 7.5 Vpp, Ω_{max}=7.7 rps. Black squares: linear interpolation of continuous measurements. Yellow symbols: measurements obtained from translation measurements of Section 5. Dashed line: theoretical prediction.

4.3 Torques observed on cells

While the previous example concerns solid objects, the application of a torque on living cells may also induce their rotation. Movie S4† is a first illustration of this possibility with the rotation of a WBC observed in a microfluidic device containing no reflector, surrounded by other RBCs rotating at a lower velocity. Other measurements performed on single and clusters of RBCs are shown in Fig. 9. While the overall trend is reminiscent of a sine function, rotations are only observable when φ is sufficiently different from 0 and π, suggesting that a minimum shear stress is required to induce a rotation. When comparing these results with those obtained with solid Janus beads, we evidence a systematic threshold for the rotation to occur. To complement these data, we recorded the arrangements of large collections of RBCs under acoustic excitation, shown in Fig. 10. From these images, and thanks to the field depth of the microscope, we see that two arrangements of RBCs are possible. Those that appear darker and

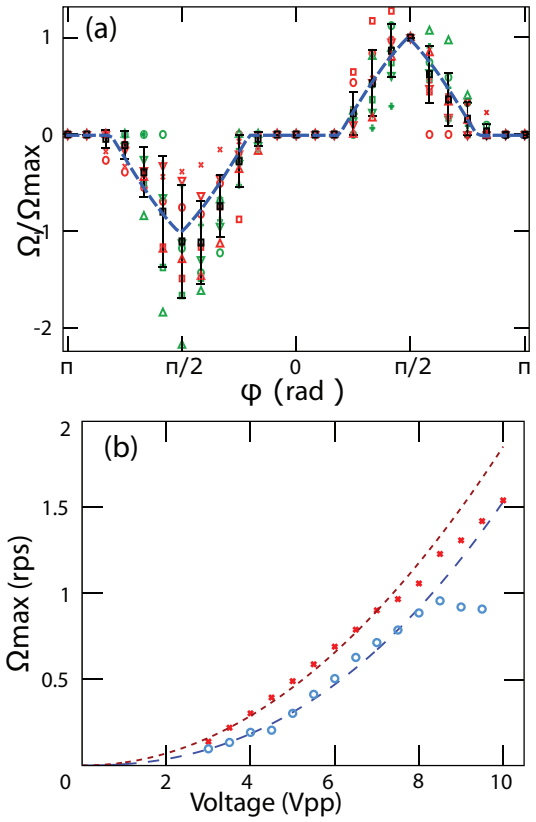

Fig. 9 Rotation velocity of RBCs clusters in a device with a glass reflector at $f_0 = 37.1$ MHz. Measurements performed by imposing constant differences $\phi_x^{\uparrow} - \phi_x^{\downarrow}$ and $\phi_y^{\leftarrow} - \phi_y^{\rightarrow}$ to avoid the motion of the particles. (a) Rotation velocity normalized to maximum value versus applied phase measured for 10 different RBC clusters. Dashed line: model assuming an acoustic viscous torque and a friction due to acoustic radiative forces on non spherical clusters. Black squares represent average and error bars are $\pm\sigma$. (b) Rotation velocity versus applied voltage for a large cluster (in red) and for an isolated RBC (in blue). Dashed lines are power law fits with exponents 2 for the RBC cluster and 2.3 for the single RBC.

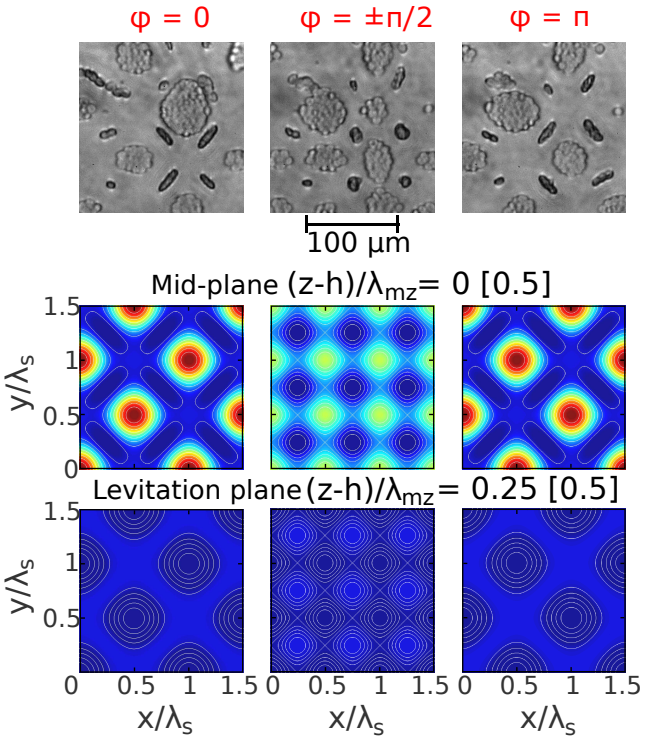

Fig. 10 Upper row: transmission microscope images of RBCs, excited at $0 = 37.1$ MHz and 10 Vpp for all IDTs and for 3 different values of φ while keeping $\phi_y^{\leftarrow} - \phi_y^{\rightarrow}$ and $\phi_x^{\uparrow} - \phi_x^{\downarrow}$ constant (see also Movie S5). Middle and bottom rows: results of 3D numerical simulations of acoustic potentials in the horizontal planes (see *supporting information SI2*) at a height z/λ_{fz}=0 [1/2] or in the levitation planes $z/\lambda_{fz} = 1/4\,[1/2]$ using $f_1 = 0.11$ [39] and $f_2 = 0.05$. The same colormap is used for both plots.

focused on the images correspond to RBCs that can preferentially rotate and that, we think, are trapped in planes with forces similar to those on the emitting $LiNbO_3$ surface. The other RBCs form thin clusters one cell thick that are trapped in levitation planes in which the radial forces are much weaker according to numerical simulation presented in the same figure. In practice, the distance between these two planes is no larger than 11 µm. To confirm this, we observed that under reduced flow and for a distance between the glass slide and the $LiNbO_3$ of about 110±10 µm, four levels of levitation clearly builds up, suggesting a height closer to 100 µm for $\theta_R = 22°$ and $\lambda_{fz} = 22$ µm. This suggests the following interpretation: RBCs trapped in mid-planes are in region where radiation forces are particularly strong and anisotropic. As a consequence, shape effects are particularly important and single particles and clusters tend to align along the minima of the acoustic potential.

To make this idea quantitative, we propose a naive model that compares the viscous torque to the torque induced by radiation forces on an elongated object made of two spheres of radii a separated by a distance 2ℓ and making an angle α with axis $\mathbf{e}_x$ (see Fig. 11b). At the same time the spheres are attracted to the central pressure node, the anisotropy of the potential well is responsible for forces being alternatively negative and positive and therefore for a total torque. Expanding eqn (11) for small values of $k_s\ell$ assuming $p_{0x} = p_{0y} = p_0$ and an isotropic substrate leads to the following approximation for the potential:

$$U^{\text{rad}} = E_{\text{ac}} \mathcal{V} \left\{ -3f_2 + k_s^2 \ell^2 \left(f_1 \sin(2\alpha)\cos(\varphi) + 3\Phi \right) \right\} \tag{14}$$

while the torque is

$$\begin{aligned} \Gamma^{\text{rad}} &= 2E_{\text{ac}} \mathcal{V} \frac{\partial}{\partial \alpha} U^{\text{rad}} \mathbf{e}_z \\ &= 4E_{\text{ac}} \mathcal{V} k_s^2 \ell^2 f_1 \cos(3\alpha)\cos(\varphi)\mathbf{e}_z \end{aligned} \tag{15}$$

For the torque due to streaming, we introduce a fictitious potential $U^{\text{streaming}}$ such that

$$\begin{aligned} \Gamma^{\text{streaming}} &= E_{\text{ac}} \mathcal{V} \frac{\partial}{\partial \alpha} U^{\text{streaming}} \mathbf{e}_z \\ &= 9E_{\text{ac}} \mathcal{V} \frac{\delta_\eta}{\rho_0} \sin(\varphi) \mathbf{e}_z \end{aligned} \tag{16}$$

in agreement with eqn (8), leading to $U^{\text{streaming}} = E_{\text{ac}} \mathcal{V} \frac{\delta_\eta}{\rho_0} \sin(\varphi)\alpha$. Then, plotting the reduced acoustic potential $(2U^{\text{rad}} + U^{\text{streaming}})/E_{\text{ac}}\mathcal{V}$ like in Fig. 11a for different values of the phase, we get a qualitative explanation. When φ is small, the driving torque due to streaming is not strong enough to overcome the radiation forces and oblong particles tend to align along the acoustic potential which, according to Fig. 6, corresponds to $\alpha = \pm\pi/4$. When φ increases, the driving torque gets stronger while the acoustic potential becomes almost anisotropic. The oblong particle starts to rotate with a solid like friction, and almost freely when $\varphi = \pm\pi/2$. This picture clearly agrees with the shapes observed in Fig. 10 of elongated clusters of RBCs for values of φ different from $\pm\pi/2$. With the parameters of Fig. 11, the rotation velocity is expected to be or

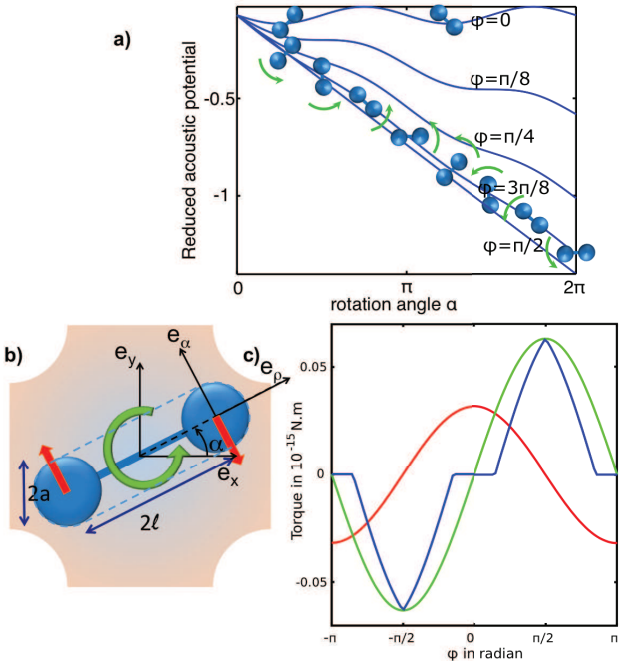

Fig. 11 a) Sketch of the total effective acoustic potential $(2U^{\text{rad}}+U^{\text{streaming}})/E_{\text{ac}}\mathscr{V}$ for two spheres of radii $a=4\,\mu$m separated by a distance $\ell=10\,\mu$m, and put in rotation via acoustic streaming. For $\varphi=0$, we show the two preferred orientations of the oblong particle. For $\varphi\geq\pi/8$, rotations are possible. Parameters: $p_{0x}=p_{0y}=10^5$ Pa , $f_1=0.11$ and $f_2=0.05$. b) Scheme of the radiative and the streaming acoustic torques on an elongated object represented by two distant spheres. c) Green curve: streaming torque $\Gamma^{\text{streaming}}$ calculated for a single sphere of radius $a=4\,\mu$m at the center according to eqn (8). Red curve: amplitude of the acoustic torque Γ^{rad} create by radiative forces. Blue curve: Effective torque obtained by subtracting the absolute value of the radiative torque from the torque due to acoustic streaming. The plateau is the region where rotations are hindered by shape effects of the particle.

order of 1 rps for pressure amplitudes of 10^5 Pa, a typical value in these experiments. Since both radiation forces and acoustic streaming are proportional to E_{ac}, we predict the same for the rotation velocity, as confirmed from measurements of Fig. 9, which shows dependencies close to square laws between Ω and applied voltages. However, there is no hint that the amplitudes of the torques due to both mechanisms should be similar in general.

5 Simultaneous control of particle translation and rotation

5.1 Principle

In this last section, we want to illustrate the potential of the present work to control simultaneously the rotation of translation of particles. For this purpose, we consider the vibration amplitude of the crystal surface due to two counter propagating waves, say along $\mathbf{e}_{\text{x}}$, as sketched in Fig. 2. The total complex amplitude of the displacement is:

$$\underline{\xi}_s(x)=\xi_{\mathbf{0x}}\sin\left(k_{\text{x}}x+(\phi_x^{\uparrow}-\phi_x^{\downarrow})/2\right)\exp\left(-i\left(\omega t-(\phi_x^{\uparrow}+\phi_x^{\downarrow})/2\right)\right) \quad (17)$$

Eqn (17) shows that the SSAW depends spatially on $(\phi_x^{\uparrow}-\phi_x^{\downarrow})/2$, while its temporal phase is set by $(\phi_x^{\uparrow}+\phi_x^{\downarrow})/2$ along direction $\mathbf{e}_{\text{x}}$, and correspondingly along $\mathbf{e}_{\text{y}}$. Thus, a clever adjustment of IDT individual phase can advantageously open a control of both the translation and rotation of particles. In this respect, the case considered by Busse *et al.* [26] is somehow trivial, since it corresponds to $\phi_y^{\rightarrow}=\phi_y^{\leftarrow}=0$ and $\phi_x^{\downarrow}=\phi_x^{\uparrow}=\varphi$, leading to a constant spatial phase shift, meaning that the beads stay in the position they have reached, while the total phase lag is $(\phi_x^{\uparrow}+\phi_x^{\downarrow})/2-(\phi_y^{\leftarrow}+\phi_y^{\rightarrow})/2=\varphi$ corresponding to a rotation with total phase φ. This is consistent with Fig. 8, with the minima of acoustic potential and the maxima of the torques coinciding whatever the value of φ is, with in practice some slight fluctuation of beads positions that may be due to imperfectly matched amplitudes.

Another interesting situation is that employed in Ref. [6] and reproduced here, in which the phases are initially equal ($\phi_y^{\rightarrow}=\phi_y^{\leftarrow}$ and $\phi_x^{\downarrow}=\phi_x^{\uparrow}$), while a small frequency shift δf is imposed on IDT$_y^{\rightarrow}$. After a time t, the position of the particle initially located in x_0 is:

$$x(t)=x_0+(\phi_x^{\uparrow}-\phi_x^{\downarrow})\lambda_{\text{x}}/4\pi \qquad \text{with} \qquad (\phi_x^{\uparrow}-\phi_x^{\downarrow})=2\pi\delta f t \quad (18)$$

As a consequence, the particle drifts linearly with time along direction $\mathbf{e}_{\text{x}}$, at a velocity $\delta f\lambda_{\text{x}}/2$.[6] Accordingly, we get for the phase lag for the stationary wave along axis $\mathbf{e}_{\text{x}}$ respective to $\mathbf{e}_{\text{y}}$ $\varphi=\text{cst}-\pi\delta f t$. Thus, while the particle is moving in the lab frame, it also rotates along an axis perpendicular to the channel plane, at a rotation velocity which depends on the local value of φ.

5.2 Measurements

We present in Fig. 12a the measurement of the successive positions of Janus beads in an acoustic device without acoustic reflector and plot the trajectory of its center of mass in Fig. 12b. As follows from a comparison with the linear fit shown in blue, the bead translates almost linearly with time (see Movie S6† showing the displacement of the bead and Movie S7 corresponding to the numerical simulation), with small deviations. At the same time, while the bead is moving, it keeps on rotating, alternating clockwise and anti-clockwise directions. Plotting in Fig. 12b the rotation speed, we observe a characteristic sine behavior as a function of φ, with slightly higher peaked valued near $\phi_x^{\uparrow}-\phi_x^{\downarrow}=\pm\pi$ that we attribute to undesired reflexions between electrode pairs.

5.3 Discussion

To further exemplify the previous approach, we show in Fig. 13 the potential field phase obtained from eqn (11) and eqn (18) and its time evolution (see also Movie S7†). As φ evolves, we see the continuous deformation of the potential landscape, and the progressive displacement of a fictitious trapped bead symbolized by the white disk, provided the displacement is not hindered by the drag force exerted on the bead. A more complex situation is illustrated by Movie S3 in which we observe the behavior of multiple beads trapped in the same potential minimum. When a triplet of 3 beads forms in a plane parallel to the substrate, a rotation is observed, at a speed comparable to that of a single

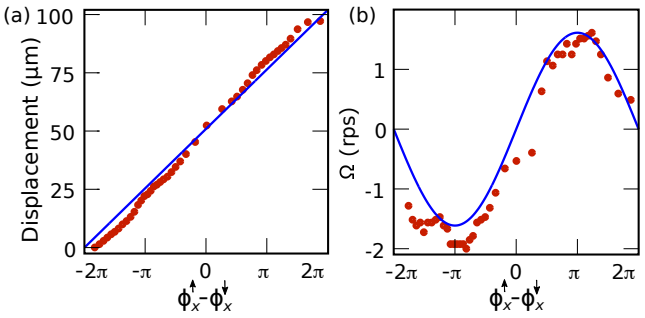

Fig. 12 Measurement of the rotation of a ⊘10 µm JANUS bead at the frequency $f_0 = 36.3$ MHz on $\text{IDT}_x^{\uparrow}$, $\text{IDT}_y^{\rightarrow}$, and $\text{IDT}_y^{\leftarrow}$, and $f_x^{\downarrow} = f_0 + \delta f$ with $\delta f = 0.05$ Hz on $\text{IDT}_x^{\downarrow}$. Excitation voltage 8 Vpp for IDT pair along axis $\mathbf{e}_x$ and 6 Vpp along axis $\mathbf{e}_y$, in a cavity without glass reflector. (a) Position of the bead after each turn as a function of the phase between emitters $\phi_x^{\uparrow} - \phi_x^{\downarrow}$. Error bars are typically ±4 µm per point. (b) Instant velocity after each rotation as a function of the phase between emitters.

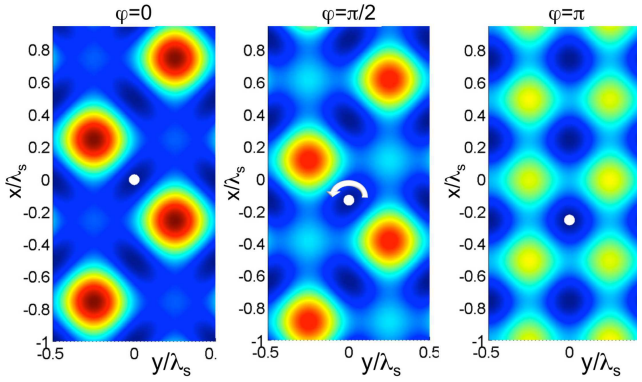

Fig. 13 Simulation of the potential map for a Janus bead in translation in a microfluidic chamber.

bead. For a doublet, this rotation is impossible or irregular. This suggests a common phenomenology for clusters and single objects: When the viscous torques are strong enough, objects tend to rotate under the action of viscous acoustic torques (see Hahn *et al.*.[42] for recent computations of the viscous torque for non spherical objects), while shape effects tend to make them align to the anisotropic potential wells. Such effect had already been evidenced and used by Zeng *et al.*[43] to oriente carbon nanotubes aggregates along preferred directions while varying the respective amplitudes between the two orthogonal directions. Now, the case of living cells is more interesting in this respect, since the objects may also be deformable and could adapt their shapes to the potential created by radiation forces at the same the viscous stress imposes a torque. This may provide a unique tool to probe their viscoelastic properties but the present study is too early to draw such conclusion. The recent work by Riaud *et al.*[44] is another important step in the same direction, since it allows the manipulation of individuel objects, which is not possible in the current geometry.

6 Conclusion

We have described a new non contact handling principle allowing for the simultaneous translation and reorientation of microparticles based on acoustic forces and torques. The working mechanism is shown to be very general and to hold for a large range of frequencies and geometries. The amplitude of forces involved (pN and more) suggests that this tool may be used to manipulate objects in the micrometer range or larger, and opens the possibility to combine micro mechanical assembly, positioning and rotation, including for biological material. We have obtained experimental evidences of this principle using for the first time the emission of surface acoustic waves emitted by a single $LiNbO_3$ sample. Developing the analogy with optical tweezers, we think we have obtained a new functionality similar to an optical rotator,[45] opening the way to a large set of applications.

7 Acknowledgements

We would like to thank Alexandre Reinhardt from CEA-Leti for helping in the design of SAW resonators. This research has benefited from a support from the European Research Council under the European Community's Seventh Framework Programme(FP7/2007-2013) ERC Grant Agreement Bubbleboost no. 614655.

References

1 P. Glynne-Jones and M. Hill, Lab on a Chip, 2013, **13**, 1003–1010.
2 Y. Huang, S. Joo, M. Duhon, M. Heller, B. Wallace and X. Xu, Analytical chemistry, 2002, **74**, 3362–3371.
3 M. Zborowski and J. J. Chalmers, Analytical chemistry, 2011, **83**, 8050–8056.
4 T. Franke, S. Braunmuller, L. Schmid, A. Wixforth and D. A. Weitz, Lab Chip, 2010, **10**, 789–794.
5 A. Ashkin, J. Dziedzic, J. Bjorkholm and S. Chu, Optics letters, 1986, **11**, 288–290.
6 S. B. Q. Tran, P. Marmottant and P. Thibault, Applied Physics Letters, 2012, **101**, 114103.
7 X. Ding, S.-C. S. Lin, B. Kiraly, H. Yue, S. Li, I.-K. Chiang, J. Shi, S. J. Benkovic and T. J. Huang, Proceedings of the National Academy of Sciences, 2012, **109**, 11105–11109.
8 L. Rayleigh, The London, Edinburgh, and Dublin Philosophical Magazine and Journal of Science, 1882, **14**, 186–187.
9 G. Maidanik, The Journal of the Acoustical Society of America, 1958, **30**, 620–623.
10 A. Garbin, I. Leibacher, P. Hahn, H. Le Ferrand, A. Studart and J. Dual, The Journal of the Acoustical Society of America, 2015, **138**, 2759–2769.
11 M. Padgett, J. Courtial and L. Allen, Physics Today, 2004, **57**, 35–40.
12 B. T. Hefner and P. L. Marston, The Journal of the Acoustical Society of America, 1999, **106**, 3313–3316.
13 R. Marchiano and J.-L. Thomas, Physical Review E, 2005, **71**, 066616.

14 R. Wunenburger, J. I. V. Lozano and E. Brasselet, New Journal of Physics, 2015, **17**, 103022.

15 H. He, M. E. J. Friese, N. R. Heckenberg and H. Rubinsztein-Dunlop, Phys. Rev. Lett., 1995, **75**, 826–829.

16 M. E. J. Friese, T. A. Nieminen, N. R. Heckenberg and H. Rubinsztein-Dunlop, Nature, 1998, **394**, 348–350.

17 C. P. Lee and T. G. Wang, The Journal of the Acoustical Society of America, 1989, **85**, 1081–1088.

18 A. Lamprecht, T. Schwarz, J. Wang and J. Dual, The Journal of the Acoustical Society of America, 2015, **138**, 23–32.

19 T. Valier-Brasier, C. Poulain et al., Lab on a Chip, 2016, **16**, 2532–2539.

20 H. Bruus, Lab on a Chip, 2012, **12**, 1014–1021.

21 K. Volke-Sepúlveda, A. O. Santillán and R. R. Boullosa, Physical review letters, 2008, **100**, 024302.

22 R. Shilton, M. K. Tan, L. Y. Yeo and J. R. Friend, Journal of Applied Physics, 2008, **104**, 014910.

23 H. Li, J. Friend and L. Yeo, Biomedical Microdevices, 2007, **9**, 647–656.

24 D. Baresch, J.-L. Thomas and R. Marchiano, The Journal of the Acoustical Society of America, 2013, **133**, 25–36.

25 A. Riaud, J.-L. Thomas, E. Charron, A. Bussonnière, O. B. Matar and M. Baudoin, Physical Review Applied, 2015, **4**, 034004.

26 F. Busse and T. Wang, The Journal of the Acoustical Society of America, 1981, **69**, 1634–1638.

27 J. J. Campbell and W. R. Jones, Sonics and Ultrasonics, IEEE Transactions on, 1968, **15**, 209–217.

28 W. Soluch and M. Lysakowska, IEEE Transactions on Ultrasonics, Ferroelectrics and Frequency Control, 2005, **52**, 145–147.

29 I. Bernard, Ph.D. thesis, Université Grenoble Alpes, 2016 - 201 pages.

30 J. Nye and M. Berry, Proceedings of the Royal Society of London A: Mathematical, Physical and Engineering Sciences, 1974, pp. 165–190.

31 A. Riaud, J.-L. Thomas, M. Baudoin and O. B. Matar, Physical Review E, 2015, **92**, 063201.

32 A. Warner, M. Onoe and G. Coquin, The journal of the acoustical society of America, 1967, **42**, 1223–1231.

33 D. Ciplys and R. Rimeika, Ultragarsas" Ultrasound", 1999, **33**, 14–20.

34 J. J. Campbell and W. R. Jones, Journal of Applied Physics, 1970, **41**, 2796–2801.

35 T. Honegger, O. Lecarme, K. Berton and D. Peyrade, Journal of Vacuum Science & Technology B, Nanotechnology and Microelectronics: Materials, Processing, Measurement, and Phenomena, 2010, **28**, C6I14–C6I19.

36 L. Gor'kov, Soviet Physics Doklady, 1962, p. 773.

37 O. Sapozhnikov and M. Bailey, The Journal of the Acoustical Society, 2013, **133**, 661–676.

38 P. B. Muller, M. Rossi, Á. Marín, R. Barnkob, P. Augustsson, T. Laurell, C. J. Kaehler and H. Bruus, Physical Review E, 2013, **88**, 023006.

39 P. Augustsson, R. Barnkob, C. Grenvall, T. Deierborg, P. Brundin, H. Bruus and T. Laurell, Proceedings of MicroTAS, 2010, **14**, 1337–1339.

40 P. Augustsson, J. T. Karlsen, H.-W. Su, H. Bruus and J. Voldman, Nature communications, 2016, **7**, 11556.

41 Q. Liu and A. Prosperetti, Journal of fluid mechanics, 2010, **657**, 1–21.

42 P. Hahn, A. Lamprecht and J. Dual, Lab on a Chip, 2016, **16**, 4581–4594.

43 Q. Zeng, L. Li, H. L. Ma, J. Xu, Y. Fan and H. Wang, Applied Physics Letters, 2013, **102**, 213106.

44 A. Riaud, M. Baudoin, O. Bou Matar, L. Becerra and J.-L. Thomas, Phys. Rev. Applied, 2017, **7**, 024007.

45 M. K. Kreysing, A. Fritsch, C. Dietrich, J. R. Guck, J. A. Kńs et al., Optics express, 2008, **16**, 16984–16992.

46 N. Nama, R. Barnkob, Z. Mao, C. J. Kähler, F. Costanzo and T. J. Huang, Lab on a Chip, 2015, **15**, 2700–2709.

47 A. Haake, Ph.D. thesis, Swiss Federal Institute of Technology Zurich, 2004 - 149 pages (see model page 44 and following).